hv photonics

MDPI

Type of the Paper (Article)

Broadband absorption in patterned metal/weakly-absorbing-spacer/metal with graded photonic super-crystal

Steve Kamau[1], Safaa Hassan[1], Khadijah Alnasser[1], Hualiang Zhang[2], Jingbiao Cui[1], and Yuankun Lin[1, 3, *]

[1] Department of Physics, Univ. of North Texas, Denton, TX 76203, USA; stevekamau@my.unt.edu (S.K.); SafaaHassan@my.unt.edu (S.H.); KhadijahAlnasser@my.unt.edu (K.A.); Jingbiao.Cui@unt.edu (J.C.)
[2] Department of Electrical & Computer Engineering, Univ. of Massachusetts Lowell, Lowell, MA 01854, USA; hualiang_zhang@uml.edu (H.Z.)
[3] Department of Electrical Engineering, Univ. of North Texas, Denton, TX 76203, USA.
* Correspondence: yuankun.lin@unt.edu (Y.L.); Tel.: +1-940-565-4548

Abstract: It is challenging to realize complete broadband absorption of near-infrared in thin optical devices. In this paper, we studied high light absorption in two devices: a stack of Au-pattern/insulator/Au-film and a stack of Au-pattern/weakly-absorbing-material/Au-film where Au-pattern is structured in graded photonic super-crystal. We observed multiple-band absorption, including one near 1500 nm, in a stack of Au-pattern/spacer/Au-film. The multiple-band absorption is due to the gap surface plasmon polariton when the spacer thickness is less than 30 nm. Broadband absorption appears in the near-infrared when the insulator spacer is replaced by a weakly absorbing material. E-field intensity was simulated and confirmed the formation of gap surface plasmon polaritons and their coupling with Fabry–Pérot resonance.

Keywords: light absorption; gap surface plasmon polariton; Fabry–Pérot resonance; graded photonic super-crystal; broadband absorption; metal/insulator/metal.

1. Introduction

The absorption of light, especially the total light absorption (TLA) in sub-wavelength thin layer stacks or patterned stacks, has been intensively studied for applications in lasers, photodetectors, solar energy harvesting, metal structural coloring, nanoscale environmental sensing, surface-enhanced Raman scattering from individual molecules, and other applications [1-11]. In two-layer or three-layer dielectrics/metal stacks, the refractive index of the dielectric materials has been carefully selected [11-15] in order to meet the phase condition for a destructive interference of light reflected from the interfaces of multiple layer stacks or critical coupling of resonances [16-24]. Plasmonic TLA with zero transmission and zero reflection has been observed [5-9, 25-26] in patterned metal-insulator-metal (MIM) stacks where light can easily couple with surface plasmons to form surface plasmon polaritons (SPPs) following the physics rule of momentum conservation. The patterned MIM consists of top-layer metallic pattern, continuous spacer-layer and metallic bottom-layer. The wavelength of plasmonic TLA was determined by the continuous-layer gap plasmon resonators without strict conditions for the refractive index of materials, in contrast to the strict condition for thin film stacks [11-15].

Broadband TLA has been desired for many applications. In order to achieve broadband plasmonic TLA, super-lattice, complex motifs or multiple resonators have been placed in a unit cell of MIM structures [25-31]. An array of chirped MIM resonators has been used to achieve broadband response [27]. Multiplexed plasmonic resonances in metallic dual-lattices have been used for broadband detector [25,26]. A super-lattice with a periodic array of 4 differently sized circles [6] or squares [28] in a unit cell in MIM has successfully generated broadband plasmonic TLA. Metasurface with multiple resonators

Citation: Lastname, F.; Lastname, F.; Lastname, F. Title. *Photonics* **2021**, *8*, x. https://doi.org/10.3390/xxxxx

Received: date
Accepted: date
Published: date

Publisher's Note: MDPI stays neutral with regard to jurisdictional claims in published maps and institutional affiliations.

Copyright: © 2021 by the authors. Submitted for possible open access publication under the terms and conditions of the Creative Commons Attribution (CC BY) license (http://creativecommons.org/licenses/by/4.0/).

in MIM has been studied for the same purpose. Examples include multiple resonators of various size/shape of squares and circles [29], eight pairs of gold nano-resonators in the complex unit cell [30], and gradient metasurfaces comprising a periodic arrangement of metal nanobricks [31].

A recently discovered graded photonic super-crystal (GPSC) can have a very large unit super-cell with two sets of motifs: the rod size (or hole size) decreases gradually along one direction in one set of motifs while the other set increases their sizes gradually [32-41]. The spatially gradient motifs are arranged on a square lattice with a small period and graded regions in GPSC have a large period and their own symmetry. The GPSC can have dual period and dual symmetry [32-42]. Due to the gradient two-set motifs in the unit super-cell, GPSCs can be used to enhance the broadband light trapping in Si solar cell and broadband light extraction from organic light emitting diode [37-41]. Various GPSCs with different symmetries and unit super-cells have been fabricated through the interference lithography by two sets of multiple beams arranged in a cone geometry [32-36].

In this paper, we simulated the light absorption in Au GPSC on Au film, Au-GPSC/insulator/Au-film, and Au-GPSC/lossy-spacer/Au film. We observed multiple-band absorption in Au-GPSC/insulator/Au-film. Especially the appearance of the absorption band near 1500 nm is due to the gap SPP in [1,1] direction. Broadband absorption has been observed when a weakly absorbing material is used between Au-GPSC and Au-film.

2. Simulation methods

Fig. 1(a) shows a schematic of to-be-simulated GPSC MIM structure where two sets of motifs are represented by orange and golden cylinders, respectively. Radii of cylinders decrease then increase along the golden arrow while they increase then decrease along the dashed orange arrow. The GPSC can be obtained by interference lithography [32-36] or e-beam lithography [42]. The E-beam exposure control program used the interference pattern as an input [42]. The eight-beam interference intensity as a function of location r is calculated from Eq. 1:

$$I(r) = \langle \sum_{i=1}^{8} E_i^2(r,t) \rangle + \sum_{i<j}^{8} E_i E_j e_i \cdot e_j cos\left[\left(k_j - k_i\right) \cdot r + (\delta_j - \delta_i) \right]. \quad (1)$$

where k is the wave vector, δ is the initial phase, E and e is the electric field strength and polarization, respectively. The four inner beams and four outer beams have their wave vectors of: {k1…4}={k(sin(7.1°)cos(45+n×90)°, sin(7.1°)sin(45+n×90)°, cos(7.1°)), {k5…8}={k(sin(47.9°)cos(45+n×90)°, sin(47.9°)sin(45+n×90)°, cos(47.9°)), respectively, where n=0,1,2,3. Using an UV source with a wavelength=367 nm, the small period Λ_s equals approximately $2\pi/(2k\sin(47.9°)\times\sin45)$=350 nm. The big period can be approximately estimated by $\Lambda_b = 2\pi/(k\sin(7.1°)\sqrt{2})$=6·350 nm. Thus there are 6×6 cylinders in the unit super-cell as indicated by a dashed red square in Fig. 1. A step function was used to generate Au GPSC: permittivity of Au, which was obtained from a reference [43], was applied when I(r) was larger than a threshold intensity I_{th}, and air when $I(r) < I_{th}$. The thickness of insulator or lossy insulator (dark blue) is H and Au film is in light blue in Fig. 1(a) in the stacks of Au GPSC/insulator/Au film, and Au GPSC/lossy insulator/Au film. For the simulation of Au GPSC on SiO_2 film, the Au film was removed. We used a finite-difference time-domain (FDTD) open-source software tool MIT MEEP program [44] to simulate the reflection, transmission and E-field. These simulations were performed at Amazon Web Service through cloud-based parallel computations using 36-core virtual machines.

3. Multiple-band absorption in Au/SiO_2/Au patterned with GPSC

Fig. 1(b) shows the simulated reflection (R) and transmission (T) from Au GPSC on dielectric SiO_2 (without the Au film). The extinction (E) is obtained by E = 1-T-R. The transmission spectrum shows a low transmission window between 400 and 600 nm. There is a

low reflection window between 400 and 720 nm in the reflection in Fig. 1(b). The calculated extinction shows a sharp peak at 613 nm and a broad band centered around 557 nm, similar to the plasmonic features observed in gold nanorods [45]. There are weak peaks around 391, 440 and 775 nm. In GPSC, the cylinders on the edge of the unit super-cell have almost same sizes and percentage of these cylinders over total number of cylinders is high. The size of cylinders becomes smaller or bigger near the center and these cylinders has a low percentage over the total number of cylinders. The bigger the size of the cylinders, the larger the plasmonic resonance wavelength following Equation (2) [6,45]:

$$D\,\frac{2\pi}{\lambda}\,n_{eff} = k\,\pi - \theta \qquad (2)$$

where D is the dimeter of cylinders, n_{eff} is the effective index for the SPP, k is an integer number and θ is the phase shift due to the SPP mode reflection. The diameter of cylinders on the edge is approximately 90 nm [42] corresponding to a localized surface plasmonic resonance wavelength of 558 nm [3] and coupled surface plasmonic resonance wavelength around 583 nm assuming reflection phase θ = 0.29 and k = 1 in Eq. (2) [6]. The plasmonic resonance wavelength can reach 793 nm for the large cylinder with a diameter of 158 nm. The high extinction between 500 and 640 nm is in agreement with the high percentage of cylinders at the edge over the total.

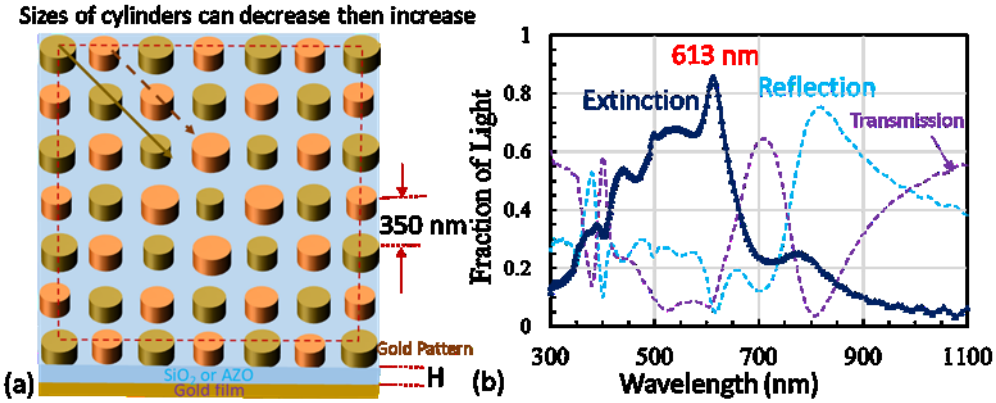

Figure 1. (a) Schematic of 6Λs×6Λs unit cell of GPSC with gold cylinders. (b) Simulated reflection, transmission and extinction for Au GPSC on a glass slide.

When the Au film is added below the SiO_2 spacer as a metal/insulator/metal structure patterned with GPSC, as shown in Fig. 1(a), multiple absorption bands appear above 620 nm as shown in Fig. 2(a), besides the broadband absorption between 400-600 nm. The absorption peaks locate at 624, 841 and 1464 nm when the thickness of SiO_2 is 10 nm. These three peaks increase in wavelength as indicated as dashed red, blue and purple arrows as the thickness of spacer increases from 10 to 15 and 30 nm. These three peaks have wavelength of (699, 904, 1625 nm) and (819, 988, 1776 nm) for the space thickness of 15 and 30 nm, respectively. These three peaks can be assigned as gap SPP following Equation (3) which is similar to Eq. (2) [6,45,46]:

$$P_{n,m}\,\frac{2\pi}{\lambda}\,n_{eff-Au-Spacer} = k\,\pi - \theta \qquad (3)$$

where P is the propagation length along [n,m] direction, $n_{eff\text{-}Au\text{-}Spacer}$ is the effective index for the SPP at the interface of gold film and SiO_2. The effective refractive index, $n_{eff\text{-}Au\text{-}Spacer}$ can obtained from Equation (4) [46]:

$$n_{eff-Au-Spacer} = \sqrt{\frac{\varepsilon_{Au}\varepsilon_{spacer}}{\varepsilon_{Au}+\varepsilon_{spacer}}} \qquad (4)$$

where ε_{Au} and ε_{Spacer} are the permittivity of gold and SiO_2, respectively. In a direction of [n,m]=[1,0] and using k=1 and reflection phase θ = 0.29, the gap SPP wavelength is calculated to be 650 nm using Eq.(3) and Eq. (4). The gap SPP wavelength is calculated to be 858 and 1653 nm in a direction of [n,m]=[1,1] for the propagation distance of $\sqrt{2}\Lambda_s$ and $2\sqrt{2}\Lambda_s$, respectively. The calculated SPP wavelengths are (650, 858, 1653 nm), comparing with the simulated SPP wavelengths of (624, 841 and 1464 nm) for a spacer thickness of 10 nm in Au/SiO_2/Au patterned with GPSC. When the thickness is increased, these three peaks are red-shifted. It should be mentioned that the effective index for gap plasmon depends on the MIM spacer thickness in metamaterial MIM structures [47-49].

When the thickness of spacer SiO_2 reaches 60 nm, the peak around 1450 nm becomes very weak as shown in Fig. 2(b). Further increasing the thickness to 90 and 120 nm, the peak completely disappears due to the weak confinement of the gap SPP with a large gap and a long propagation length [45]. The gap SPPs do still exist but they are not efficiently coupled to the resonator.

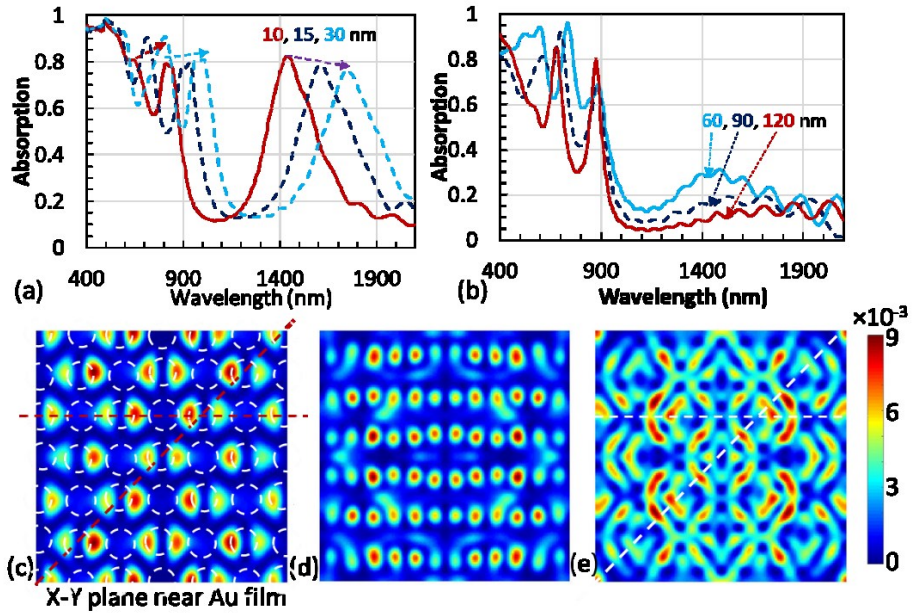

Fig. 2, (a) Multiple-band absorption due to gap SPP in Au/SiO_2/Au patterned with GPSC when the SiO_2 thickness is 10 (solid red line), 15 (dashed dark-blue line) and 30 nm (dashed light-blue line). (b) Absorption in Au/SiO_2/Au patterned with GPSC when the SiO_2 thickness is 60 (solid light-blue line), 90 (dashed dark-blue line) and 120 nm (solid red line). (c) E-field intensity in X-Y plane inside the spacer near Au film (c), in the middle of the spacer (d), and inside the spacer near Au GPSC (c), in a stack of Au-GPSC/20-nm-SiO_2/Au film. These E-field intensities are excited by a Gaussion source with a central wavelength of 1400 nm.

Fig. 2(c) shows E-field intensity in X-Y plane inside the spacer near Au film in a stack of Au-GPSC/20-nm-SiO_2/Au film. The dashed white circles indicate the lattice location for Au GPSC. The dashed red lines indicate the horizontal and [1,1] directions. Within 20 nm from the Au GPSC, E-field intensity has a pattern with a symmetry similar to GPSC lattice. The E-field oscillate near locations for one set of lattices where blue cylinders locate in Fig. 1(a) in x-direction following x-polarization of light. Fig. 2(d) shows E-field intensity in X-Y plane in the middle of the spacer. Gap SPP modes are clearly observed. The E-field intensity in X-Y plane inside the spacer near Au GPSC is shown in Fig. 2(e). Both oscillations in horizontal and [1,1] directions in E-field intensity are presented with an eye-guidance from the dashed white lines. Due to two sets of lattices in GPSC, this is reasonable to have an E-field coupling along [1,1] direction with the same set of motif in the lattice, comparing with diffraction orders of (1,1), (1,−1), (−1,−1) and (−1,−1) observed in the diffraction

pattern from Al GPSC [42]. Due to the fact that there is SPP coupling near Au GPSC in Fig. 2(e) while the coupling in [1,1] direction in Fig. 2(c) is weak with a distance from Au GPSC, the gap SPP coupling with resonators in a long propagation distance in [1,1] direction will become weak when the thickness of spacer is increased. That's why the absorption peak around 1600 nm disappears in Fig. 2(a) and Fig. 2(b) when the spacer thickness is increased to be larger than 60 nm.

3. Broad-band absorption in Au/absorbing-spacer/Au patterned with GPSC

In order to achieve a broad absorption in near-infrared, we replace SiO_2 with a weakly absorbing material that has a complex refractive index n+ik with k<<n. The dielectric function of the material can be obtained by the Drude-Lorentz oscillator model in Equation (5):

$$(\omega) = \varepsilon_b - \frac{\omega_p^2}{\omega^2 + i\Gamma_p\omega} + \frac{f_1\omega_1^2}{\omega_1^2 - \omega^2 - i\Gamma_1\omega} \quad (5)$$

where the background permittivity $\varepsilon_b = 3.358$, the plasma frequency $\omega_p = 0.41$ eV, the carrier relaxation rate $\Gamma_p = 0.04$ eV, and $f_1 = 1.69$, representing the strength of the Lorentz oscillator with center frequency $\omega_1 = 0.64$ eV and relaxation $\Gamma_1 = 0.2$ eV. These permittivity parameters are adopted from the spectra ellipsometry on AZO with different Al-doping [50]. AZO or ITO is popular as an electrically-tunable and transparent conducting material for tunable MIM devices [51]. Fig. 3 shows calculated real (n) and imaginary (k) parts of the refractive index in the wavelength range between 500 and 4500 nm. k<<n as shown in the figure. The imaginary part k increase from zero at low wavelength to 0.002 at 1260 nm, to 0.005 at 1698 nm, to 0.01 at 2120 nm, and then to 0.02 at 2630 nm. Correspondingly, the real part n decreases from 1.82, to 1.78, 1.74, 1.69 and then to 1.61. We also plot n and k in Fig. 3 for carrier relaxation rate Γ_p =0.14 eV and 0.28 eV while other parameters are same. The carrier relaxation rate in Drude model in Eq. (5) is related to the optical loss. When Γ_p increases, k increases in Fig. 3.

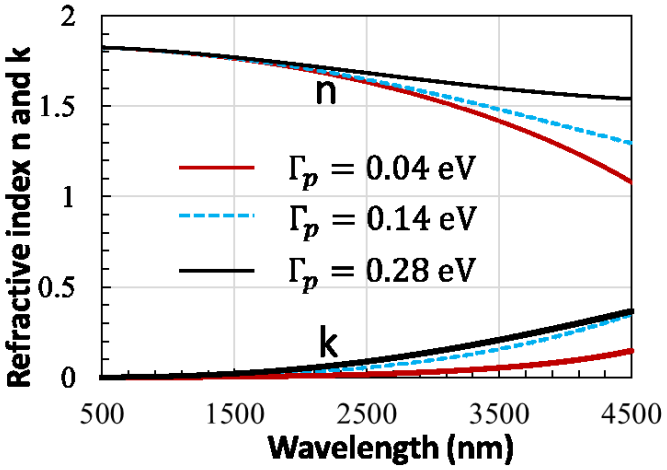

Figure. 3. The real (n) and imaginary (k) parts of refractive index for wavelength range between 500 and 4500 nm for carrier relaxation rates of 0.04, 0.14 and 0.28 eV in Eq. (5).

Fig. 4(a) shows absorption for spacer thickness of 80, 120 and 350 nm in a stack of Au-GPSC/weakly-absorbing-spacer/Au-film. Broadband absorption appears for the thickness of 80 and 120 nm around 1400-2300 nm where peaks is disappearing in Fig. 2(b). Considering the refractive index and Fabry–Pérot (F-P) effect, optical path length of 120-nm×1.5 (1.5 is the refractive index) in Fig. 2(b) corresponds to optical path length of 100-nm×1.8 in Fig. 4(a). The difference in absorption in near-infrared between two figures can be due to the weakly absorbing spacer used in Fig. 4(a).

The F-P resonance in Fig. 4 can form inside the spacer between Au-GPSC and Au film with a possible F-P cavity length (FPCL) in Equations (6-8) [52-54]:

$$F-P\ Cavity\ Length = FPCL = 2\sqrt{\left(\frac{\Lambda_{n,m}}{2}\right)^2 + T^2} \quad (6)$$

$$F-P\ Cavity\ Length = FPCL = 2\sqrt{\left(\frac{D}{2}\right)^2 + T^2} \quad (7)$$

$$F-P\ Cavity\ Length = FPCL = 2T \quad (8)$$

where T is the thickness of the spacer, D is the diameter of cylinder in GPSC, $\Lambda_{n,m}$ is the lattice period in [n,m] direction. Eq. (6) is for F-P resonance diffracted by the GPSC grating from different directions while Eq. (7-8) is for F-P between Au-cylinders and Au-film as shown inserts in Fig. 4(c) for type II and type I, respectively. The formation of the F-P resonance meets the following condition in Equation (9) [53,55]:

$$FPCL\ \frac{2\pi}{\lambda}\ n_{spacer} = k\,\pi - \varphi_{top} - \varphi_{bottom}\,,\ \ m = 1,2,3\ldots \quad (9)$$

where φ_{top} and φ_{bottom} are the additional phase shifts at top and bottom surfaces, respectively, due to the reflection and penetration depth. With a penetration depth of 26 nm around 1900 nm in Au, φ=0.06. We use $\varphi_{top}+\varphi_{bottom}$=0.29+0.06 for the path in Eq. (6-7) and $\varphi_{top}+\varphi_{bottom}$=0.06+0.06 for the path in Eq. (8). Using these additional phase shifts, the calculated wavelength for the absorption peak is close to the simulated one.

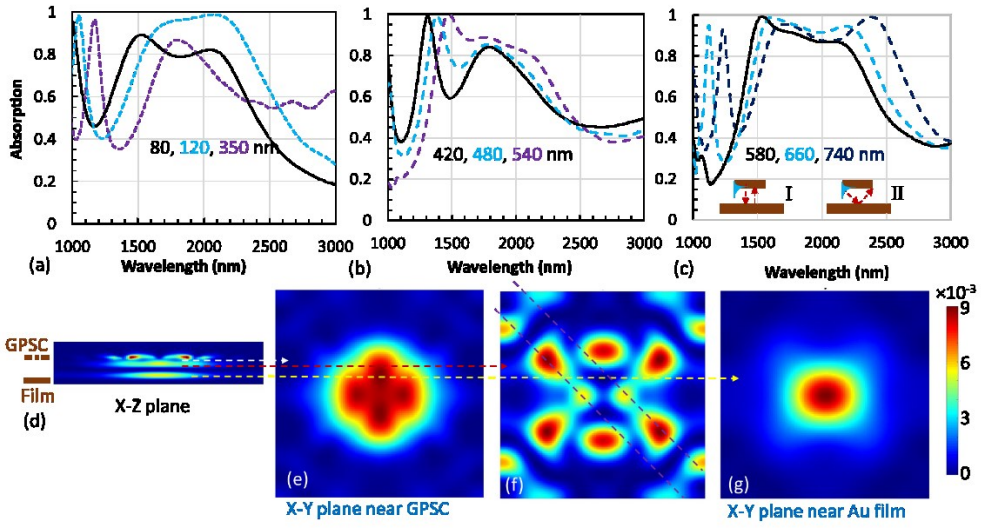

Figure. 4. Simulated absorption in a stack of Au-GPSC/weakly-absorbing-spacer/Au-film with a spacer thickness of (80, 120, 350 nm) (a), (420, 480, 540 nm) (b), and (580, 660, 740 nm) (c). (d) E-field intensity in a cross section in X-Z plane for a space thickness of 350 nm. (e-g) E-field intensity in a cross section in X-Y plane through z-locations indicated by dashed white, red and yellow arrows, respectively. These E-field intensities are excited by a Gaussion source with a central wavelength of 1900 nm.

Based on Eq. (6-9), SPP and F-P coupling in [1,1] direction gives an absorption centered around 1962 nm for the spacer thickness of 120 nm, in agreement with the simulated broadband absorption wavelength between 1600 and 2200 nm, and the central wavelength of 1975 nm indicated by dashed green square in Fig. 5. For the thickness of 420 nm in Fig. 4(b), the absorption is calculated to be 1780 nm using Eq. (8). The absorption is

around 2200 and 2050 nm for the spacer thickness of 580 nm in Fig. 4(c) using Eq. (7) and Eq. (8), respectively.

Fig. 4(d) shows E-field intensity in a cross section in X-Z plane for a space thickness of 350 nm in a stack of Au-GPSC/weakly-absorbing-spacer/Au-film. The E-field intensity is high near the center of unit super-cell of GPSC and F-P resonance appears between Au-GPSC and Au-film. Fig. 4(e) shows E-field intensity in a cross section in X-Y plane through z-locations indicated by the dashed white arrow (just below Au-GPSC). A square pattern appears following the GPSC symmetry. In the middle of the spacer, E-field intensity shows oscillations along [1,1] direction as indicated by dashed purple lines. The light is reflected by Au film at the center of unit super-cell as shown in Fig. 4(g). Thus, the coupling of SPP and F-P resonance leads toward a broadband absorption in near-infrared in the stack of Au-GPSC/weakly-absorbing-spacer/Au-film. For thin device applications, a space thickness of 120 nm in Fig. 4(a) can have a broadband absorption in near-infrared.

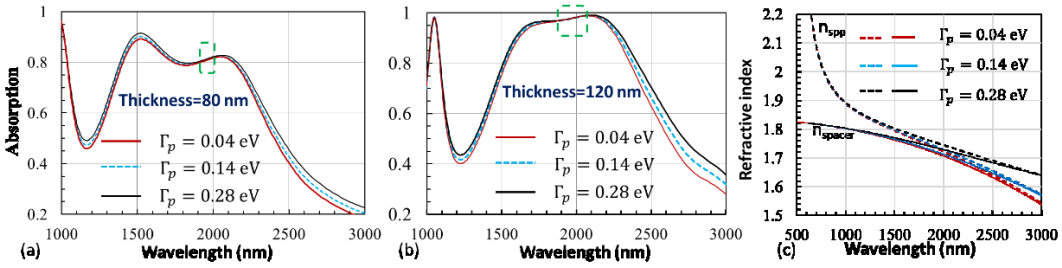

Figure. 5. Simulated absorption in a stack of Au-GPSC/weakly-absorbing-spacer/Au-film with a spacer thickness of 80 nm (a) and 120 nm (b) for carrier relaxation rates of 0.04, 0.14 and 0.28 eV in Eq. (5) for AZO spacer. (c) Dispersion of refractive index n_{spp} and n_{AZO} with carrier relaxation rates of 0.04, 0.14 and 0.28 eV in Eq. (5) for AZO spacer.

5. Discussion

Although super-lattice, complex motifs or multiple resonators have been placed in a unit cell of MIM structures by other research group [25-31], the broad absorption around 1400-2100 nm has not been reported. We believe the coupling of SPP with GPSC resonators in [±1, ±1] directions plays a key role in the appearance of broad absorption band around 1400-2100 nm in our GPSC based MIM as evidenced by the E-field intensity here and reported laser diffraction in [±1, ±1] from GPSC pattern [42]. Due to the dual lattice feature as indicated by arrows in Fig. 1(a) for GPSC, the SPP is forced to propagate and resonate in [1,1] direction. Due to different diameters for cylinders in GPSC, the SPP has a broadband resonance.

We believe the material dispersion also plays a role in coupling of SPP with F-P resonance in the spacer. Adopting the permittivity in Eq. (5) and in Fig. 3 for AZO, we simulate the absorption of Au-GPSC/weakly-absorbing-spacer/Au-film for carrier relaxation rates of 0.04 (red line), 0.14 (blue dash) and 0.28 eV (black line), as shown in Fig. 5(a) and 5(b) for the spacer thickness of 80 nm and 120 nm, respectively. The absorption increases with increasing k (increasing Γ_p) as expected in both Fig. 5(a) and 5(b). However, the absorption is almost same between the wavelength of 1916 and 2014 nm in Fig. 5(a) and between 1860 and 2090 nm in Fig. 5(b), as indicated by dashed green rectangle and square in the figure, respectively. These dashed green rectangle and square are centered at 1965 and 1975 nm, respectively. It indicates that the SPP wavelength is around 1970 nm and it is mainly related to the Au permittivity and GPSC structure. The broadband coupling between SPP and F-P resonance can be understood from the dispersion of n_{spp} and n_{spacer} as shown in Fig. 5(c). These n_{spp} and n_{spacer} are very close and change with wavelength in almost same slope between 1700 and 2200 nm.

6. Conclusion

In summary, we have observed multi-band absorption in a stack of Au-GPSC/SiO_2/Au-film. The absorption band near 1500 nm is assigned to the gap SPP in [1,1] direction. This feature appears in the stack patterned in GPSC due to its dual-lattice structure and coupling of SPP along one set of lattice in [1,1] direction. Broadband absorption has been observed in a stack of Au-GPSC/weakly-absorbing-spacer/Au-film due to SPP and F-P resonance in [1,1] direction. E-field intensity has been simulated for both stacks where SPP and F-P resonance have been confirmed. The E-field intensity has confirmed the formation of gap SPP near 1500 nm when the spacer thickness is below 30 nm.

Author Contributions: Y.L., J.C. and H.Z. conceived the concepts; Y.L., S.K. and S.H. designed simulations; S.K., S.H. and K.A. performed the simulations; Y.L., S.K. and S.H. analyzed the data and wrote the paper. All authors read and comment on the manuscript.

Funding: This work is supported by research grants from the U.S. National Science Foundation under Grant Nos. CMMI- 1661842 and 1661749.

Conflicts of Interest: The authors declare no conflict of interest. The funders had no role in the design of the study; in the collection, analyses, or interpretation of data; in the writing of the manuscript, or in the decision to publish the results.

Data Availability Statement: Data will be available upon request.

Acknowledgments: We thank Noah Hurley for improving the English in the manuscript.

References

1. Zhao, J.; Wang, Y.; Zhu, Y.; Zhang, W.; and Yu, Y. Lithography-free flexible perfect broadband absorber in visible light based on an all-dielectric multilayer structure. *Opt. Lett.* **2020**, 45, 5464-5467.
2. Anker, J.N.; Hall, W.P.; Lyandres, O.; Shah, N.C.; Zhao, J.; and Van Duyne, R.P. Biosensing with plasmonic nanosensors. *Nat. Mater.* **2008**, 7, 442–453.
3. Cao, J.; Sun, T.; and Grattan, K.T.V. Gold nanorod-based localized surface plasmon resonance biosensors: a review, *Sensors and Actuators B: Chemical* **2014**, 95, 332-351.
4. Chong, Y.D.; Cao, L. Ge. H.; and Stone, A. D. Coherent perfect absorbers: time-reversed lasers. *Phys. Rev. Lett.* **2010**, 105, 053901.
5. Fang, Z.; Zhen, Y.R.; Fan, L.; Zhu, X.; and Nordlander, P. Tunable wide-angle plasmonic perfect absorber at visible frequencies. *Phys. Rev. B* **2012**, 85, 245401.
6. Nielsen, M.G.; Pors, A.; Albrektsen, O. and Bozhevolnyi, S.I. Efficient absorption of visible radiation by gap plasmon resonators. Opt. Express **2012**, 20, 13311–13319.
7. Luk, T.S.; Fofang, N.T.; Cruz-Campa, J.L.; Frank, I.; Campione, S. Surface Plasmon polariton enhanced ultrathin nano-structured CdTe solar cell. *Opt. Express* **2014**, 22, A1372–A1379.
8. Chen, H. Interference theory of metamaterial perfect absorbers. *Opt. Express* **2012**, 20, 7165–7172.
9. Aydin, K, Ferry, EV, Briggs, MR, Atwater, HA (2011) Broadband polarization-independent resonant light absorption using ultrathin plasmonic super absorbers. Nat. Commun **2011**, 2, 517.
10. Sun, T.; Guo, C.F.; Cao, E. M.; Akinoglu, Y.; Wang, M.; Giersig, Z.; Ren.; and Kempa,K. A broadband solar absorber with 12 nm thick ultrathin a-Si layer by using random metallic nanomeshes. *Appl. Phys. Lett.* **2014**, 104, 251119.
11. Sturmberg, B.C.P.; Chong, T.K.; Choi, D.Y.; White, T.P.; Botten, L.C.; Dossou, K.B.; Poulton, C.G.; Catchpole, K.R.; McPhedran, R.C.; and de Sterke, C.M. Total absorption of visible light in ultrathin weakly absorbing semiconductor gratings. *Optica* **2016**, 3, 556-562.
12. Ghobadi, A.; Hajian, H.; Rashed, A.R.; Butun, B. and Ozbay, E. Tuning the metal filling fraction in metal-insulator-metal ultra-broadband perfect absorbers to maximize the absorption bandwidth. *Photon. Res.* **2018**, 6, 168-176.
13. Kats, M.A.; Blanchard, R.; Genevet, P.; and Capasso, F. Nanometer optical coatings based on strong interference effects in highly absorbing media. *Nat. Mater.* **2013**, 12, 20–24.
14. Kats, M.A.; Byrnes, S.J.; Blanchard, R.; Kolle, M.; Genevet, P.; Aizenberg, J.; and Capasso, F. Enhancement of absorption and color contrast in ultra-thin highly absorbing optical coatings. *Appl. Phys. Lett.* **2013,** 103, 101104.
15. Yongbing, L.; Runmei, S.; Qiwen, W.; Liang, S.; Bowen, L.; and Wenhao, Z. Deducing critical coupling condition to achieve perfect absorption for thin-film absorbers and identifying key characteristics of absorbing materials needed for perfect Absorption. *Appl. Phys. Lett.* **2014**,104, 091109.
16. Ding, B.; Qiu, M.; and Blaikie, R.J. Manipulating light absorption in dye-doped dielectric films on reflecting surfaces. *Opt. Express* **2014**, 22, 25965–25975.

17. Song, H.; Guo, L.; Liu, Z.; Liu, K.; Zeng, D. Ji.; Zhang, N.; Hu, H.; Jiang, S.; and Gan, Q. Nanocavity enhancement for ultra-thin film optical absorber. *Adv. Mater.* **2014,** 26, 2737–2743.
18. Li, Z.; Butun, S.; and Aydin, K. Large-area lithography-free super absorbers and color filters at visible frequencies using ultrathin metallic films. *ACS Photonics* **2015**, 2, 183–188.
19. Li, Z.; Palacios, E.; Butun, S.; Kocer, H.; and Aydin, K. Omnidirectional broadband light absorption using large- area ultrathin lossy metallic film coatings. Sci. Rep. 2015, 5, 15137.
20. Lee, K.T.; Seo, S.; Lee, J.Y.; and Guo, L.J. Strong resonance effect in a lossy medium-based optical cavity for angle robust spectrum filters. Adv. Mater. 2014, 26, 6324–6328.
21. Streyer, W.; Law, S.; Rooney, G.; Jacobs, T.; and Wasserman, D. Strong absorption and selective emission from engineered metals with dielectric coatings. Opt. Express 2013, 21, 9113–9122.
22. Lee, K.T.; Ji, C.; and Guo, L.J. Wide-angle, polarization-independent ultrathin broadband visible absorbers. Appl. Phys. Lett. 2016, 108, 031107.
23. Kocer, H.; Butun, S.; Li, Z.; and Aydin, K. Reduced near-infrared absorption using ultra-thin lossy metals in Fabry-Perot cavities. Sci. Rep. 2015, 5, 8157.
24. Mirshafieyan, S.S.; Luk, T.S.; and Guo, J. Zeroth order Fabry-Perot resonance enabled ultra-thin perfect light absorber using percolation aluminum and silicon nanofilms. Opt. Mater. Express 2016, 6, 1032-1042.
25. Zhang, B.; Hendrickson, J.; and Guo, J. Multispectral near perfect metamaterial absorbers using spatially multiplexed plasmon resonance metal square structures. J. Opt. Soc. Am. B 2013, 30, 656–662.
26. Hendrickson, J.; Guo, J. B.; Zhang, W. B.; and Soref, R. Wideband perfect light absorber at midwave infrared using multiplexed metal structures. Opt. Lett. 2012, 37, 371–373.
27. Song, Y.; Wang, C.; Lou, Y.; Cao, B.; Li, X. Near-perfect absorber with ultrawide bandwidth in infrared region using a periodically chirped structure. Opt. Commun. 2013, 305, 212.
28. Palanchoke, U.; Boutami, S.; Pocas, S.; Rochat, N.; Goudon, V.; and Rabaud, W. Influence of dimensional variation of metal-insulator-metal stack in spectral response. Opt. Mater. Express 8, 2494-2509 (2018).
29. Nagarajan, A.; Vivek, K.; Shah, M.; Achanta, V.G.; and Gerini, G. A Broadband Plasmonic Metasurface Superabsorber at Optical Frequencies: Analytical Design Framework and Demonstration. Adv. Optical Mater. 2018, 6, 1800253.
30. Azad, A.K.; Kort-Kamp, W.J.M.; Sykora, M.; Weisse-Bernstein, N.R.; Luk, T.S.; Taylor, A.J.; Dalvit D.A.R.; & Chen H. Metasurface Broadband Solar Absorber. Scientific Reports 2016, 6, 20347.
31. Pors, A.; Albrektsen, O.; Radko I.R.; & Bozhevolnyi, S.I. Gap plasmon-based metasurfaces for total control of reflected light. Sci. Rep. 2013, 3, 2155.
32. Lowell, D.; Lutkenhaus, J.; George, D.; Philipose, U.; Chen, B.; and Lin, Y. Simultaneous direct holographic fabrication of photonic cavity and graded photonic lattice with dual periodicity, dual basis, and dual symmetry. Opt. Express **2017**, 25, 14444-14452.
33. Lowell, D.; Hassan, S.; Adewole, M.; Philipose, U.; Chen, B.; and Lin, Y. Holographic fabrication of graded photonic supercrystals using an integrated spatial light modulator and reflective optical element laser projection system. Appl. Opt. **2017**, 56, 9888.
34. Lowell, D.; Hassan, S.; Sale, O.; Adewole, M.; Hurley, N.; Philipose, U.; Chen B.; and Lin, Y. Holographic fabrication of graded photonic super-quasi-crystal with multiple level gradients. Applied Optics 2018, 57, 6598.
35. Hassan, S.; Sale, O.; Lowell, D.; Hurley, N.; and Lin, Y. Holographic fabrication and optical property of graded photonic supercrystals with a rectangular unit super-cell. Photonics **2018**, 5, 34.
36. Sale, O.; Hassan,S.; Hurley, N.; Alnasser, K.; Philipose, U.; Zhang, H.; and Lin, Y. Holographic fabrication of octagon graded photonic super-crystal and potential applications in topological photonics. Front. Optoelectron. 2020, 13, 12-17.
37. Hassan, S.; Lowell, D.; and Lin, Y. High light extraction efficiency into glass substrate in organic light-emitting diodes by patterning the cathode in graded superlattice with dual periodicity and dual basis. J. Appl. Phys. **2017**, 121, 233104.
38. Hassan, S.; Alnasser, K.; Lowell, D.; and Lin, Y. Effects of Photonic Band Structure and Unit Super-Cell Size in Graded Photonic Super-Crystal on Broadband Light Absorption in Silicon. Photonics **2019**, 6, 50.
39. Hassan, S.; Sale, O.; Alnasser, K.; Hurley, N.; Zhang, H.; Philipose, U.; and Lin, Y. Broadband light-matter interaction due to resonance cavities in graded photonic super-crystals. OSA Continuum **2019**, 2, 3272-3280.
40. Hassan, S.; Lowell, D.; Adewole, M.; George, D.; Zhang, H.; and Lin, Y. Extraordinary light trapping enhancement in silicon solar cell patterned with graded photonic super-crystal. Photonics 2017, 4, 50.
41. Alnasser, K.; Hassan, S.; Kamau, S.; Zhang, H.; and Lin, Y. Enhanced light extraction from organic light emitting diodes by reducing plasmonic loss through graded photonic super-crystals, J. Opt. Soc. America B 2020, 37, 1283.
42. Hassan, S.; Jiang, Y.; Alnasser, K.; Hurley, N.; Zhang, H.; Philipose, U.; Lin, Y. Generation of over 1000 Diffraction Spots from 2D Graded Photonic Super-Crystals. *Photonics* 2020, 7, 27.
43. Rakic, A.; Djurisic, A.; Elazar, J.; and Majewski, M. Optical properties of metallic films for vertical-cavity optoelectronic devices. Appl. Opt. **1998**, 37, 5271.
44. Oskooi, F.; Roundy, D.; Ibanescu, M.; Bermel, P.; Joannopoulos, J.D.; and Johnson, S.G. MEEP: A flexible free-software package for electromagnetic simulations by the FDTD method. Comput. Phys. Commun. 2010, 181, 687.
45. Pors, A.; and Bozhevolnyi, S.I. Plasmonic metasurfaces for efficient phase control in reflection. *Opt. Express* **2013**, 21, 27438-27451.

46. Maradudin, A.A.; Sambles, J.R. and Barnes, W.L. Handbook of Surface Science Volume 4: Modern Plamnonics (Elsevier, Oxford, UK, 2014).
47. Koechlin, C.; Patrick Bouchon, Fabrice Pardo, Jean-Luc Pelouard, and Riad Haïdar, Analytical description of subwavelength plasmonic MIM resonators and of their combination. Opt. Express 2013, 21, 7025-7032.
48. Toudert, J.; Rosalia Serna, Marina García Pardo, Nicolas Ramos, Ramón J. Peláez, and Belén Maté, Mid-to-far infrared tunable perfect absorption by a sub - λ/100 nanofilm in a fractal phasor resonant cavity. Opt. Express 2018, 26, 34043-34059.
49. Yu, P.; Lucas V. Besteiro, Yongjun Huang, Jiang Wu, Lan Fu, Hark H. Tan, Chennupati Jagadish, Gary P. Wiederrecht, Alexander O. Govorov, and Zhiming Wang. Broadband metamaterial absorbers. Advanced Optical Materials 2019, 1800995.
50. George, D.; Li, L.; Jiang, Y.; Lowell, D.; Mao, M,; Hassan, S.; Ding, J.; Cui, J.; Zhang, H.; Philipose, U.; Lin, Y. Localized Surface Plasmon Polariton Resonance in Holographically Structured Al-doped ZnO. *J. Appl. Phys.* **2016**, 120, 043109.
51. Park, J.; J. Kang, X. Liu, and M.L. Brongersma. Electrically tunable Epsilon-NearZero (ENZ) metafilm absorbers. Sci. Rep. 2015, 5, 15754.
52. Evans, R.N.; Seth R. Calhoun, Jonathan R. Brescia, Justin W. Cleary, Evan M. Smith, and Robert E. Peale. Far-infrared bands in plasmonic metal-insulator-metal absorbers optimized for long-wave infrared. MRS Advances Volume 2019, 4, 667-674.
53. George, D.; Adewole, M.; Hassan, S.; Lowell, D.; Cui, J.; Zhang, H.; Philipose, U.; Lin, Y. Coupling of Surface Plasmon Polariton in Al-Doped ZnO with Fabry-Pérot Resonance for Total Light Absorption. *Photonics* **2017**, 4, 35.
54. Nath, J.; Modak, S.; Rezadad, I.; Panjwani, D.; Rezaie, F.; Cleary, J.W. and Peale, R.E. Far-infrared absorber based on standing-wave resonances in metal-dielectric-metal cavity. Opt. Express **2015**, 23, 20366-20380.
55. Cui, Y.; He, Y.; Jin, Y.; Ding, F.; Yang, L.; Ye, Y.; Zhong, S.; Lin, Y.; He, S. Plasmonic and Metamaterial Structures as Electromagnetic Absorbers. Laser Photonics Rev. **2014**, 8, 495–520.